Typeset using AASTeX62-reep

Geometric Assumptions in Hydrodynamic Modeling of Coronal and Flaring Loops

Jeffrey W. Reep,[1] Ignacio Ugarte-Urra,[1] Harry P. Warren,[1] and Will T. Barnes[2,3,4]

[1]Space Science Division, Naval Research Laboratory, Washington, DC 20375
[2]National Research Council Research Associate Residing at the Naval Research Laboratory, Washington, DC 20375
[3]NASA Goddard Space Flight Center, Heliophysics Sciences Division, Greenbelt, MD 20771
[4]Department of Physics, American University, Washington, DC 20016

Abstract

In coronal loop modeling, it is commonly assumed that the loops are semi-circular with a uniform cross-sectional area. However, observed loops are rarely semi-circular, and extrapolations of the magnetic field show that the field strength decreases with height, implying that the cross-sectional area should expand with height. In this work, we examine these two assumptions directly to understand how they affect the hydrodynamic and radiative response to strong, impulsive heating events. Both the magnitude and rate of area expansion impact the dynamics directly, and we show that an expanding cross-section significantly lengthens the time for a loop to cool and drain, increases upflow durations, and suppresses sound waves. An increase in the eccentricity of loops, on the other hand, only increases the draining timescale, and is a minor effect in general. Spectral line intensities are also strongly impacted by the variation in the cross-sectional area since they depend on both the volume of the emitting region as well as the density and ionization state. With a larger expansion, the density is reduced, so the lines at all heights are relatively reduced in intensity and, because of the increase of cooling times, the hottest lines remain bright for significantly longer. Future modeling work needs to include area expansion for an accurate picture of the hydrodynamics, and future observations are needed to provide tighter constraints on the magnitude, rate, and location of the expansion or lack thereof.

Key words: Sun: atmosphere; Sun: corona; Sun: flares; Sun: transition region

1. Introduction

Field-aligned hydrodynamic loop modeling of both quiescent regions and flares typically makes simplifying assumptions about the geometry, namely that the loops are semi-circular in shape with constant cross-section along their lengths. These assumptions, however, have not been critically examined nor are they necessarily correct. Observations of loops with imagers

jeffrey.reep@nrl.navy.mil

such as the Extreme Ultraviolet Imager (EUVI, Wuelser et al. 2004) or the Atmospheric Imaging Assembly (AIA, Lemen et al. 2012) onboard the Solar Dynamics Observatory (SDO, Pesnell et al. 2012) very often show loops that are not circular (e.g. Aschwanden 2009), often appearing more elliptical, which will alter the gravitational acceleration parallel to the loop. Furthermore, since the magnetic field strength decreases from the photosphere into the corona, by the conservation of magnetic flux, we expect that the cross-sectional area of loops must expand. This expansion of the area would affect the flows along the loop drastically, which can then impact the temperatures, densities, and therefore the entire resultant spectrum of emission from the loop.

In Mikić et al. (2013), the effect of a non-uniform cross-sectional area was shown to affect the transport of energy by thermal conduction, which in turn impacts the occurrence of thermal non-equilibrium (TNE). One manifestation of TNE is the occurrence of periodic coronal rain events known to occur in active regions (Auchère et al. 2018; Pelouze et al. 2020). Rain is also seen prominently in solar flares (Jing et al. 2016; Scullion et al. 2016), but does not occur in hydrodynamic simulations of impulsive heating (Reep et al. 2020). A non-uniform area is likely an important ingredient to the production of rain, but currently poorly understood in both quiescent and flare contexts.

Imaging observations of coronal loops widths, however, do not show significant expansion across the length of coronal loops (Klimchuk 2000; Klimchuk & DeForest 2020). This lack of significant expansion is found for both flaring and non-flaring loops, and does not depend on loop length (Watko & Klimchuk 2000). As noted by Watko & Klimchuk (2000), this seemingly contradicts the observation that the magnetic field strength decreases from photosphere to corona (Gary 2001), which would necessitate an increase in the area expansion due to conservation of magnetic flux. Comparison of observed and modeled spectral line intensities observed across the solar atmosphere suggests that the area does expand in both quiescent (Warren et al. 2010b) and flaring contexts (Reep et al. 2021), but this is far from settled. In this work, we do not seek to explain this discrepancy, and we simply work with the assumption that the area may expand.

As we will show, the cooling time of a coronal loop depends directly on the area expansion, and therefore this is a possible explanation for a commonly reported problem that modeled loops cool too fast relative to observations. In both quiescent loops and flaring loops, it has been noted that the observed cooling times are too long compared to model predictions (whether in relative or absolute terms). For example, Ugarte-Urra et al. (2006) found that there was a discrepancy between the time delays observed in active regions measured with Yohkoh's Soft X-ray Telescope (SXT, Tsuneta et al. 1991) and the 195 Å channel of the Transition Region and Coronal Explorer (TRACE, Handy et al. 1999) when compared to hydrodynamic simulations. Warren et al. (2010a) found that simulations could not reproduce the long cooling phase of post-flare loop arcades observed by Hinode's X-Ray Telescope (XRT, Golub et al. 2007). Many similar flare observations have suggested that the long-lasting cooling phase of post-flare loops may be due to a number of factors, such as gradual phase heating (Qiu & Longcope 2016), turbulent suppression of thermal conduction (Bian et al. 2016; Zhu et al. 2018), and evaporative cooling (Lee et al. 2020), among other possibilities. Area expansion is one such possibility that requires further exploration.

In this work, therefore, we examine the effects of the two geometric assumptions – area expansion and loop ellipticity – and how they might affect conclusions drawn from hydrody-

namic simulations. We show that an area expansion can significantly impact both the hydrodynamic evolution of loops and the intensities of lines across the solar atmosphere, and further that the rate and location of expansion also impact the evolution. Ellipticity, on the other hand, is relatively minor, only affecting the draining time of loops.

2. Hydrodynamic Modeling

In this work, we use the HYDrodynamics and RADiation code (`HYDRAD`[1], Bradshaw & Mason 2003; Bradshaw & Cargill 2013) to solve the field-aligned hydrodynamic equations of a two-fluid plasma confined to a magnetic flux tube. `HYDRAD` assumes that the plasma consists of electrons and hydrogen (neutral or ionized), and trace elements are included as an extra term to the electron density, in the radiative loss calculation, and as an increase in the effective mass. `HYDRAD` uses full adaptive mesh refinement to spatially resolve conserved quantities in sufficient detail.

In the presence of a non-uniform cross-sectional area A, the conservation of mass, momentum, and energy are then given by:

$$\frac{\partial \rho}{\partial t} + \frac{1}{A}\frac{\partial}{\partial s}\Big(A\rho v\Big) = 0 \tag{1}$$

$$\frac{\partial}{\partial t}\Big(\rho v\Big) + \frac{1}{A}\frac{\partial}{\partial s}\Big(A\rho v^2\Big) = \frac{1}{A}\frac{\partial}{\partial s}\Big(\frac{4A\eta}{3}\frac{\partial v}{\partial s}\Big) - \rho g_{\parallel} - \frac{\partial}{\partial s}\Big(P_e + P_H\Big) \tag{2}$$

$$\frac{\partial E_e}{\partial t} + \frac{1}{A}\frac{\partial}{\partial s}\Big[A(E_e + P_e)v\Big] = -\frac{1}{A}\frac{\partial}{\partial s}\Big(AF_{ce}\Big) + v\frac{\partial P_e}{\partial s} - n_e n_H \Lambda(T) + \frac{k_B n_H}{\gamma - 1}\nu_{ie}\Big(T_H - T_e\Big) + H_e \tag{3}$$

[1] https://github.com/rice-solar-physics/HYDRAD

$$\frac{\partial E_H}{\partial t} + \frac{1}{A}\frac{\partial}{\partial s}\Big[A(E_H + P_H)v\Big] = -\frac{1}{A}\frac{\partial}{\partial s}\Big(AF_{ci}\Big) + v\frac{\partial P_e}{\partial s} + \rho v g_{\parallel} + \frac{k_B n_H}{\gamma - 1}\nu_{ie}\Big(T_e - T_H\Big) + H_H \tag{4}$$

In these equations, s is the field-aligned coordinate, t time, ρ the mass density, n the number density, v the bulk-flow velocity, $E_e = \frac{P_e}{\gamma - 1}$ the electron energy and P_e pressure, and $E_H = \frac{P_H}{\gamma - 1} + \frac{1}{2}\rho v^2$ the hydrogen energy and pressure. η is the dynamic ion viscosity, where electron viscosity is neglected, F_c is the thermal conduction, ν_{ie} the collision frequency between ions and electrons, $g_{\parallel}$ the parallel acceleration due to gravity, and $\Lambda(T)$ is the optically thin emissivity. Finally, the terms H_e and H_H are the heating rates applied to either the electrons or hydrogen.

In this work, we use the so-called VAL C chromospheric density and temperature profile (Vernazza et al. 1981), with an approximation to the optically thick radiative losses there (Carlsson & Leenaarts 2012). We use impulsive heating by an electron beam, but the major results of this paper are in the cooling phase and so do not depend strongly on the details of the heating (Winebarger & Warren 2004). The heating function is then approximated by the equations in Emslie (1978), with modifications for non-uniform ionization by Hawley & Fisher (1994). Recent work by Allred et al. (2020) has shown that this approximation is relatively inaccurate with particularly strong heating, and a solution to the Fokker-Planck equation is more suitable in general, though the approximation works well when the only force is due to Coulomb collisions of the non-thermal electrons.

3. Expanding Cross-Sectional Area

The impact of expanding cross-sections has been touched upon only sparsely in the literature of field-aligned hydrodynamic simulations. Emslie et al. (1992) examined the impact of an expanding area on the evaporative flows driven by an impulsive electron beam and how it affects observed blue-shifts of Ca XIX emission. Mikić et al. (2013) explored how the cross-sectional area affects thermal conduction and thermal non-equilibrium (TNE) in coronal loops, and Froment et al. (2018) performed an in-depth parameter space survey to understand the occurrence of TNE or coronal condensations, but found that TNE can occur in nearly any geometry. Reep et al. (2020) showed that an expanding area itself is not sufficient to cause coronal condensations (rain) in impulsively heated loops.

In this section, therefore, we examine how an expanding area can impact both the hydrodynamic evolution and the resultant irradiance at various temperatures. Since it is not well known where the expansion occurs, or the rate at which it occurs, we consider two forms of expansion: one where the cross-section increases gradually and continuously, and one where the expansion only occurs in the transition region.

3.1. *Continuous Area Expansion*

In order to better understand the effect of a non-uniform cross-sectional area, we examine four simulations with different cross-sectional area profiles, but otherwise identical parameters. We use the area expansion function from Mikić et al. (2013), which is a continuous expansion over the length of the loop, and choose values such that the the expansion from footpoint to apex is 1 (uniform), 11, 43, and 116, which span the approximate range of expected expansion factors (see Appendix A). The profiles $A(s)$ are shown at top in Figure 1. Note that the expansion used in the simulations is only a relative expansion, and does not require a physical value. We heat the loops with an electron beam with peak flux $F = 10^{10.3}$ erg s^{-1} cm^{-2}, lasting for 100 s, with a low energy cut-off of 15 keV and spectral index of 5. The heating parameters are not crucially important to examine the differences in hydrodynamic response over long time scales, and the overall evolution would be similar for other parameters. The center and bottom plots in Figure 1 show the evolution of the apex temperatures and densities in these four simulations. The total times for the loop to cool and drain after heating onset are both significantly increased with an increasing area.

Next, we examine the overall evolution of the loops. Figure 2 shows the hydrodynamic evolution along the loops (x-axis) with time (y-axis) for the electron temperature (top), electron density (center), and bulk flow velocity (bottom). The four cases are shown in order from left to right (1x, 11x, 43x, and 116x). In the velocity plots, blue indicates a flow toward the loop apex and red away from the apex, which does not necessarily correspond to a Doppler shift. Once again, it is apparent that the cooling and draining times are both significantly increased with increasing area expansion. As in Reep et al. (2020), we find that there are no coronal condensations (rain events), indicating that area expansion alone is not sufficient to produce rain. The velocity plots show two interesting features. First, as the area expansion is increased, the duration of upflows is also increased, lasting significantly longer than the assumed heating duration. Reep et al. (2018) examined the relation between upflow duration and heating duration, finding that they are approximately equal, but that study only examined uniform area loops. This should be reexamined in detail. Second, the sound waves shown at bottom left, seen as alternating up- and downflows, are suppressed with larger area expansions. As evaporative material flows up into an area of the loop with larger cross-section, the speed slows, effectively

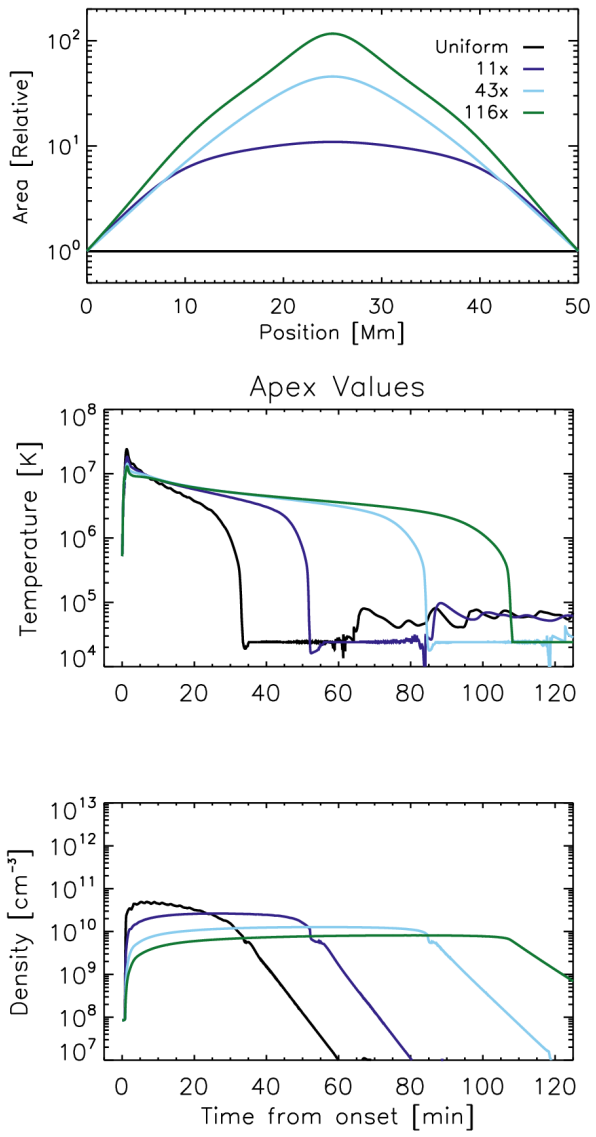

Figure 1. A comparison of the area profiles (top) used in this section and the evolution of the apex temperatures (center) and densities (bottom). We contrast four cases with four different expansion factors: uniform area, and expansions of 11, 43, and 116 from footpoint to apex of the loop. Note that the area expansion is relative, since the dynamics do not depend on the actual area magnitude, only the relative change.

causing a damping of the sound waves. Finally, we note that there is no formation of coronal condensations, rain, or prominences in any of these simulations (see also Reep et al. 2020).

We now turn to the effect on radiative emission. In each simulation, we calculate the emission measure for each grid cell at each time step, EM$= \int n_e(s)\ n_H(s)\ dV = \int n_e(s)\ n_H(s)\ A(s)\ ds$, which we then combine with the emissivities from the CHIANTI atomic database (version 10, Dere et al. 1997; Del Zanna et al. 2021). We then sum up the emission along the full length of the loop at each time step to create a time series. Note that this assumes the spectral lines are optically thin, which may not be true in general, particularly for the cooler lines.

In Figure 3, we show a comparison of irradiance light curves synthesized from these four simulations for 12 spectral lines as might be measured by the Extreme Ultraviolet Variability Experiment (EVE, Woods et al. 2012) onboard SDO, as labeled in the plots, ranging from He II 304 Å at $\log T = 4.7$ through Fe XXIV 192 Å at $\log T = 7.25$. We have assumed that the total volume, $V = \int_L A(s)\ ds$, in each simulation is equal, and we have assumed photospheric abundances (Asplund et al. 2009). It is clear that the non-uniform cross-sectional area strongly impacts the irradiance in all of these lines. First, the emission is reduced with a larger total expansion while the loop remains hot. Second, the increase in the cooling and draining times that was shown in Figure 2 is apparent in these plots, where the emission from *e.g.* Fe XVI remains relatively bright for a longer time with increasing area. Third, we note that the peak irradiance in the transition region lines (N IV, O V, O VI, Ne VII, Ne VIII, and Fe IX) is similar for each of the four area expansion factors. This spike in intensity occurs when the coronal segment of the loop cools through the line's formation temperature, and since the total loop volumes are normalized, the resultant intensities are similar. Finally, since the peak density is higher with a smaller area (see the apex densities in Figure 1), the hottest

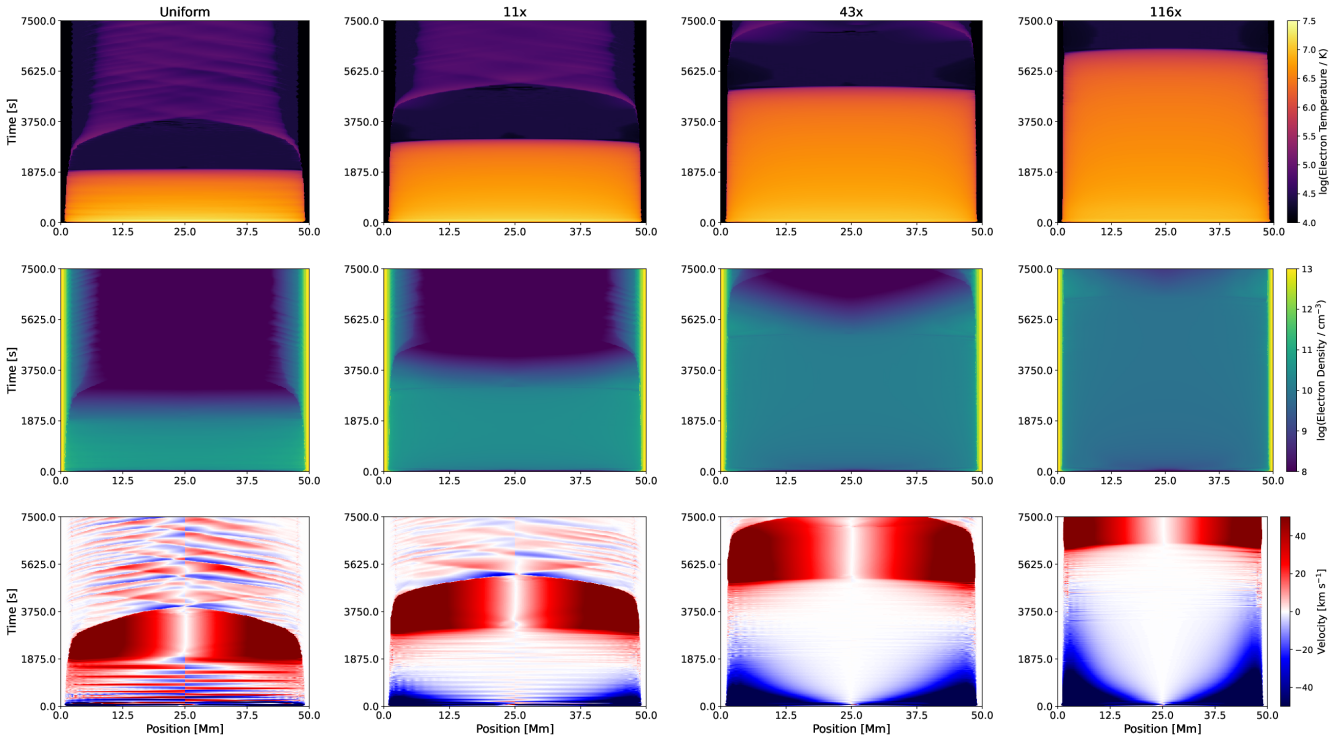

Figure 2. The evolution of the electron temperature (top), density (center), and bulk flow velocity (bottom) in four circular loops with varying cross-sectional area. From left, the total area expansion is 1 (uniform), 11, 43, and 116, corresponding to the profiles in Figure 1. The x-axis shows the position along the loop, while the y-axis shows the evolution in time. In the velocity plots, blue indicates a flow towards the apex, while red indicates a flow away from the apex, and does not necessarily correspond to a Doppler shift. The cooling time is significantly longer with increasing area, and we find approximately $\tau \propto A^{1/4}$. Evaporative upflows last for significantly longer with a larger area expansion, and sound waves are suppressed.

lines are brightest with smaller area expansions (*e.g.* Fe XXII 122 Å and Fe XXIII 133 Å), and all lines are brighter at early times with a smaller area expansion.

These plots suggest that we may be able to infer the approximate expansion factor from observed cooling times. That is, because the cross-sectional area expansion correlates well with the cooling time of the loop, and because the intensity spikes sharply when the loop cools through the formation temperature of a line, we can approximate the expansion factor by measuring the cooling time. The time to cool from, *e.g.*, Fe XVIII 94 Å to He II 304 Å increases slightly with area expansion (1.2 minutes in the uniform loop versus 3 minutes in the 116x loop). Of course, SDO/AIA channels have a relatively broad contribution so this sort of comparison requires caution.

3.2. *Transition Region Localized Expansion*

Imaging observations often show little expansion in the coronal portion of loops (Klimchuk 2000; Klimchuk & DeForest 2020), which is at odds with the decrease of the magnetic field strength from photosphere through corona that would necessitate expansion. One possible explanation for this discrepancy is that area expansion occurs mostly or only in the transition region (TR), and that any expansion in the corona is limited. We take an agnostic position in this work, and therefore additionally present a comparison of how a TR-only expansion would affect the dynamics.

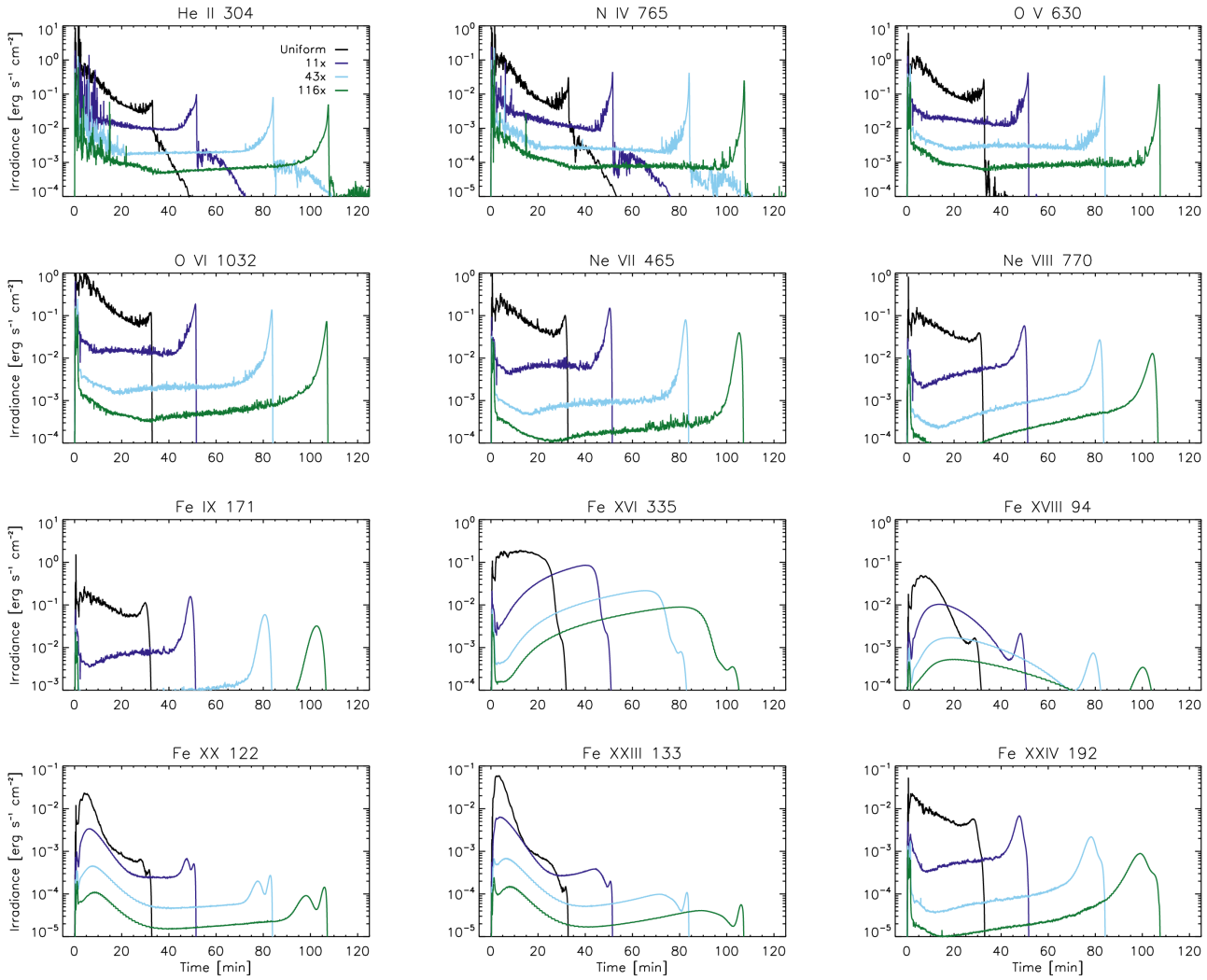

Figure 3. Synthetic irradiance time series for 12 spectral lines, as labeled (arranged by formation temperature, from coolest to hottest), as might be seen by SDO/EVE for each of the four cross-sectional area cases in Figure 1. The total volumes ($=\int_L A(s)\ ds$) have been normalized to be equal. The area expansion drastically affects the intensities of all lines at all times, both directly through the volume at a given height and indirectly through the effects on the hydrodynamics.

We quantify a TR-localized expansion using a hyperbolic tangent function, chosen *ad hoc* to simply examine this possibility. The magnetic field strength $B(s)$ near the transition region is:

$$B(s) = \frac{B_{\rm max} + B_{\rm min}}{2} - \frac{B_{\rm max} - B_{\rm min}}{2} \tanh\left(\frac{s - s_0}{2\sigma L}\right) \quad (5)$$

where where we have defined s_0 as an offset for the location of the transition region, σ is a scale height of the expansion, and L is the loop length. We assume the coronal segment of the loop has a constant magnetic field strength.

We examine three cases in this section to better understand this. We use a gradual expansion case, where the area increases continuously from the footpoint to the apex of the loop to a peak value of 10. We also compare this to two TR-confined expansion cases, one with $s_0 = 2.5$ Mm and $\sigma = 5$ Mm in Equation 5, and one with $s_0 = 1.5$ Mm and $\sigma = 3$ Mm. In all three cases, we assume a loop length of 50 Mm, and use the same heating parameters as in the previous sec-

tion. The area profiles are shown in Figure 4 at top, along with the evolution of the apex temperatures and densities (bottom). When the expansion occurs closer to the footpoint, the cooling and draining times are both reduced. The peak temperature reaches a similar value in all three cases, and peak at a similar time.

To get a fuller picture, we also present the full hydrodynamic evolution in Figure 5. The gradual case is shown at left, while the case with $s_0 = 2.5$ Mm and $\sigma = 5$ Mm is in the center, and $s_0 = 1.5$ Mm and $\sigma = 3$ Mm is at right. The change to the cooling time is apparent. Additionally, the flow profiles are somewhat modified. When the expansion is confined near the footpoints, the up-flow speeds quickly dampen as the area rapidly expands ($A\ v = \text{const}$). In contrast, when the area expands gradually, its effect on the velocity is less pronounced, and the up-flow speeds remain strong well into the coronal portion of the loop. Similarly, the suppression of sound waves which we noted in Figure 2 occurs in the gradual expansion case, but is mostly absent when the expansion is confined to the TR. Once again, no coronal condensation events occur.

Finally, we once again synthesize the irradiance as might be seen by SDO/EVE for each case to understand how the dynamics affect the radiative output. In Figure 6, we show the synthesized irradiance for the same set of 12 lines, ranging in formation temperature from $\log T = 4.7$ to 7.25. We once again normalize the total volume of each simulation. Since the cooling time is reduced when the expansion occurs near the footpoint, the coolest lines peak in intensity earlier in the TR-confined cases. The hot lines peak at similar times, but are somewhat brighter in the gradual expansion case as the density is higher (compare the apex densities in Fig. 4).

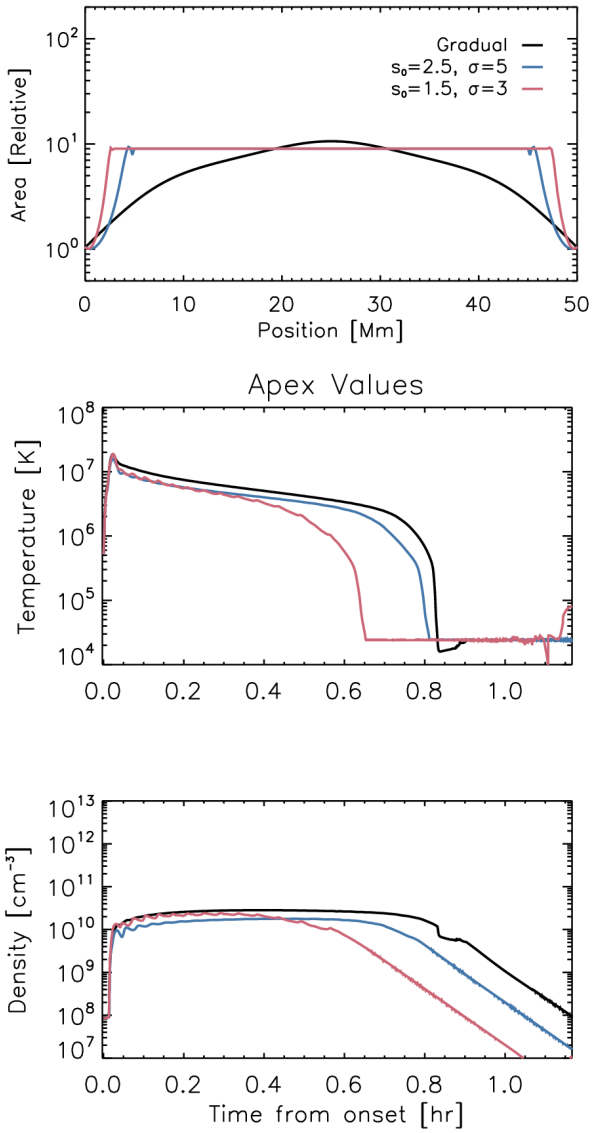

Figure 4. Similar to Figure 1, a comparison of the area profiles (top) used in this section and the evolution of the apex temperatures and densities (bottom). We contrast three cases: gradual expansion (black), TR-confined expansions with $s_0 = 2.5$ Mm and $\sigma = 5$ Mm (blue), and $s_0 = 1.5$ Mm and $\sigma = 3$ Mm (red). The cooling and draining times are reduced with expansion more confined near the TR.

4. Elliptical Loops

In this section, we examine the assumption of semi-circular loops. The gravitational acceleration parallel to the field line is given generally

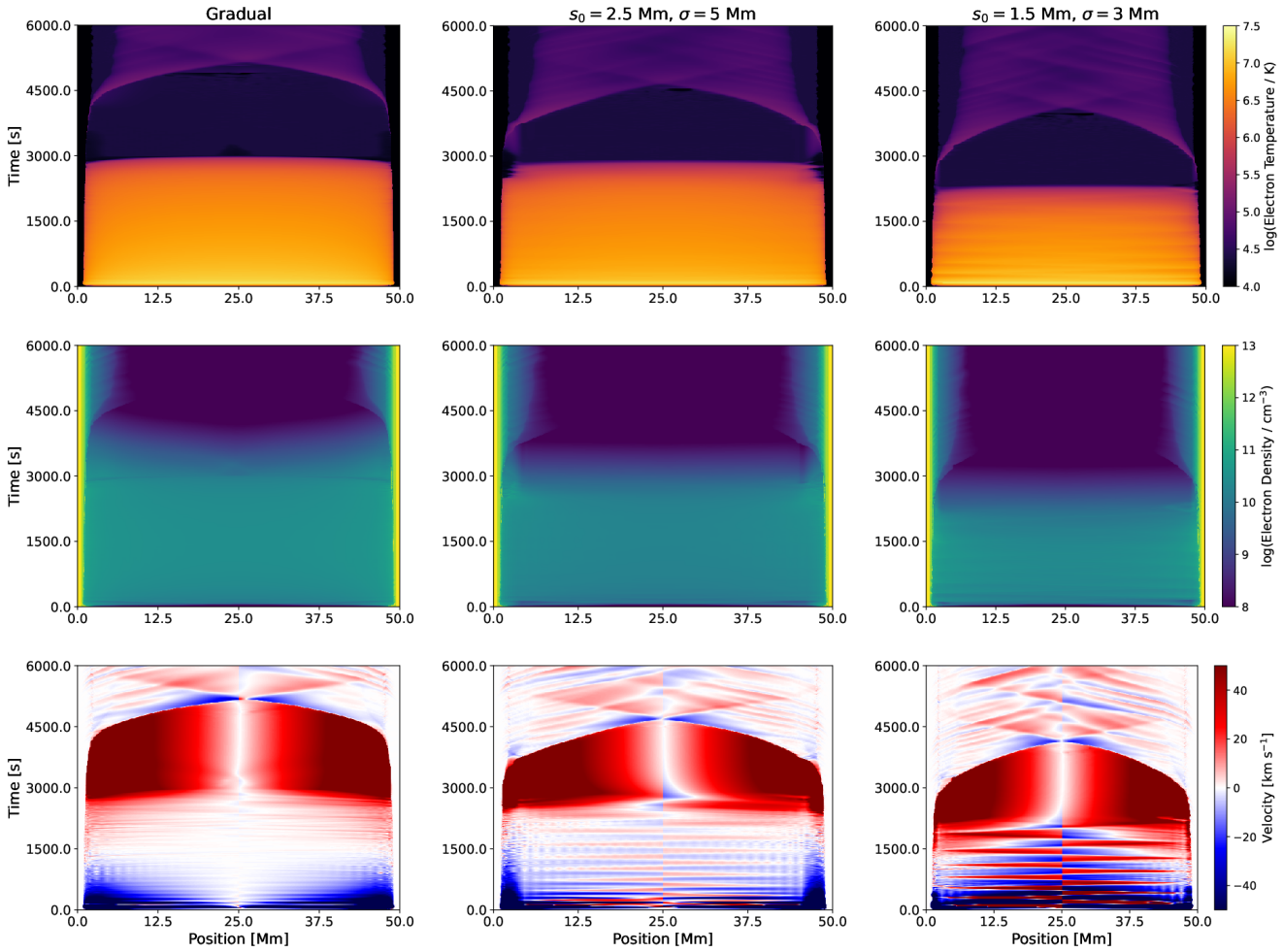

Figure 5. Similar to Figure 2, comparing three cases, gradual expansion (left), along with TR-confined expansions with $s_0 = 2.5$ Mm and $\sigma = 5$ Mm (center), and $s_0 = 1.5$ Mm and $\sigma = 3$ Mm (right). The cooling and draining times are reduced when the expansion occurs lower in the atmosphere. The up-flows become similarly confined near the location of expansion, and behaves more like a uniform-area case (compare Fig. 2).

by:

$$g_{\parallel} = g_{\odot}\left(\frac{R_{\odot}}{R_{\odot} + h\sin\theta}\right)^2 \cos\theta \qquad (6)$$

where h is the height and θ is the angle relative to the center of the loop above the surface. We derive the implementation of this for the more general case in Appendix B, and then use that in simulations to understand how it affects the dynamics.

4.1. *Comparison of Elliptical Loops*

We examine a heating rate typical of solar flare simulations. We assume that the loop is heated by an electron beam for 100 s, with a peak heating rate of $10^{10.3}$ erg s^{-1} cm^{-2}, low energy cut-off of 15 keV, and spectral index δ of 5.

Figure 7 shows a comparison of the hydrodynamic evolution of three elliptical loops. The simulation parameters are all the same except for the gravitational acceleration. The left column shows a tall loop, where the semi-major axis is oriented radially outwards from the solar surface and 3 times larger than the semi-minor axis. The center column shows a semicircular loop. The right column shows a wide loop, where the semi-major axis is oriented parallel to

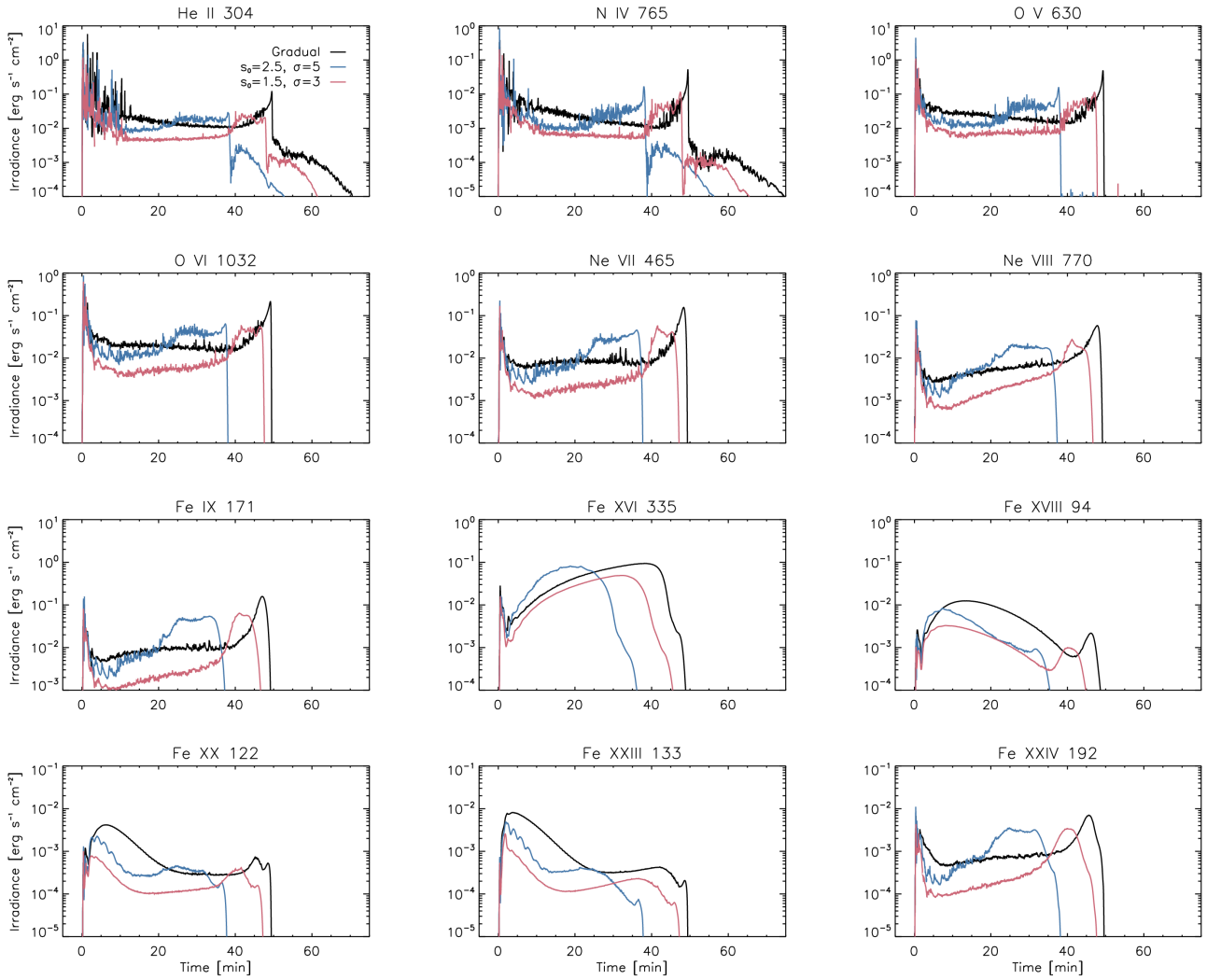

Figure 6. Similar to Figure 3, comparing three cases, gradual expansion (black), along with TR-confined expansions with $s_0 = 2.5$ Mm and $\sigma = 5$ Mm (blue), and $s_0 = 1.5$ Mm and $\sigma = 3$ Mm (red). The peak intensities are somewhat brighter in the gradual case because it has a higher density. The cool lines brighten much later in the gradual expansion case because of the increased cooling times.

the solar surface, and also 3 times larger than the semi-minor axis. The first three rows show the electron temperature, electron density, and bulk flow velocity along the loop (x-axis) as it evolves in time (y-axis). Red flows indicate motion away from the apex and blue indicates motion towards the apex. The bottom row shows a comparison of the electron temperatures and densities at the loop apex (including wide and tall loops with $a = 2b$). The overall evolution of the temperatures, densities, and velocities are nearly identical in the three cases. The only major difference is that the draining time increases somewhat with height, as might be expected for a slightly weaker gravitational acceleration.

In Figure 8, we also show the synthetic irradiance for 12 spectral lines, ranging in formation temperature from about 50 kK to 20 MK, as might be observed by SDO/EVE. We show five cases with different ellipticities, for both tall and wide loops, corresponding to the gravitational acceleration profiles in Figure 14. Unsurprisingly, since the hydrodynamic evolution is not largely impacted, the line intensities are also not

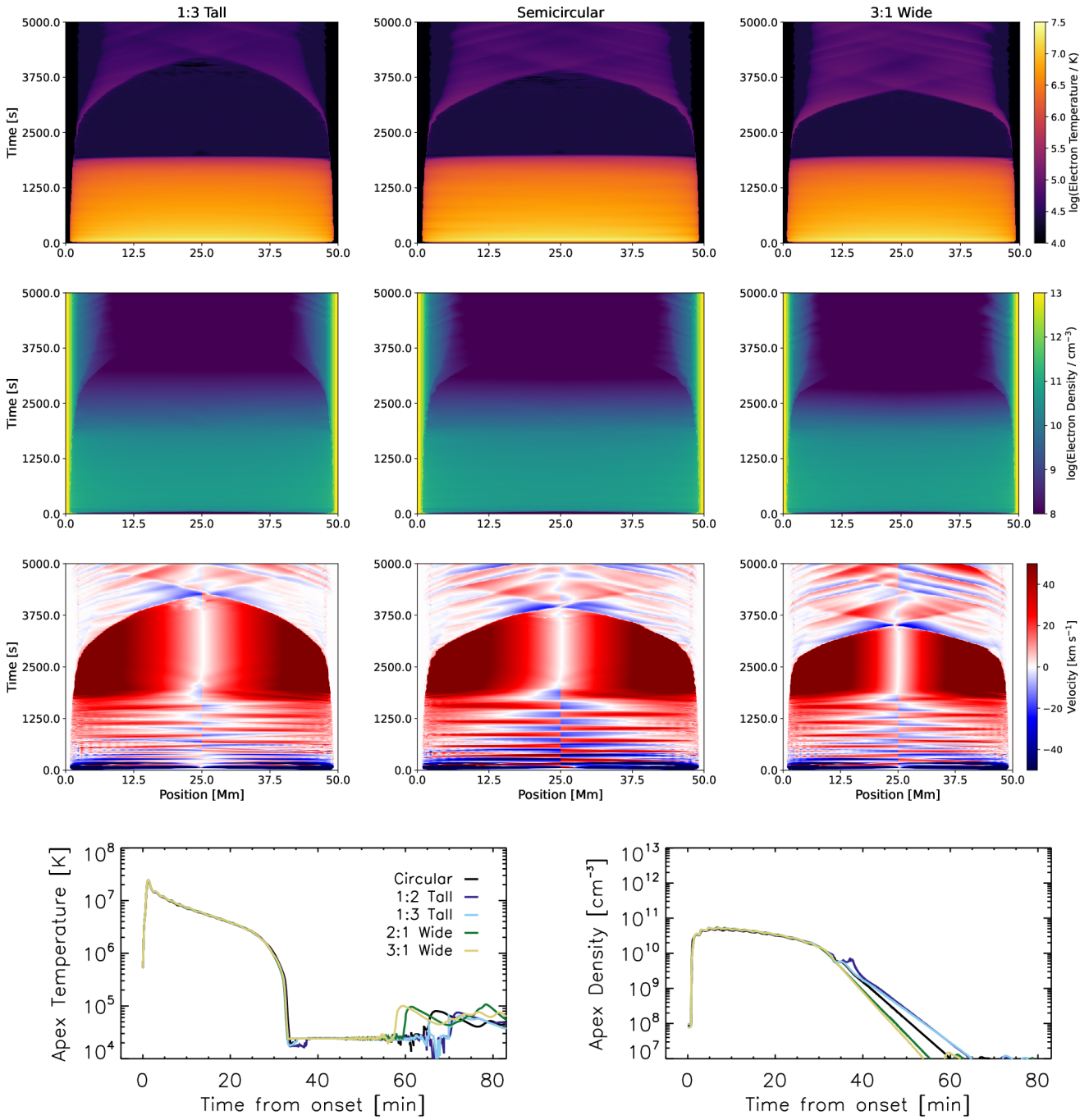

Figure 7. The overall hydrodynamic evolution in a set of elliptical flaring loops with uniform area. The left column shows a tall loop (1:3), the center a semicircular loop (1:1), and the right a wide loop (3:1). The bottom row shows a comparison of the apex temperature and density in the three cases. The draining time of the loops increases slightly with height, but the evolution is otherwise remarkably similar. Ellipticity does not strongly impact the hydrodynamics.

strongly impacted, once again indicating that the ellipticity is relatively unimportant.

5. Elliptical, Expanding Loops

In general, we expect that coronal loops are both elliptical with expanding areas. In this section, we combine the two geometrical effects to examine how this may affect the dynamics and emission. Using the same elliptical loops in the previous section, we now assume that the cross-sectional area is not uniform. Instead, we make the assumption that the magnetic field decreases with radial distance as $B \propto \frac{1}{r^2}$, and since $A \propto \frac{1}{B}$, we have $A \propto r^2$. We use a maximal expansion of precisely 10 from footpoint to apex in the circular loop. Compared to the profiles used in Figure 1, this expansion profile is more gradual with distance along the loop.

We examine simulations using both the gravity profiles in Figure 14 and area profiles in 9. Figure 10 shows the hydrodynamic evolution of these loops. The left, center, and right columns show a tall loop (3:1), circular loop (1:1), and wide loop (1:3), respectively, while the bottom two plots show the evolution of the apex temperatures and densities. Although the tall loop has the largest area expansion, the circular case has the longest cooling time. Compared to the results in Section 3, this indicates that the rate of expansion $\frac{dA}{ds}$ also affects the cooling time (see also Cargill et al. 2021), since we have already seen that the ellipticity does not impact the cooling time. The velocity profiles are also noticeably affected in these loops. In taller loops, the speed of the evaporative upflows dampens with height quickly. As the area gradually expands with height, the speed decreases due to the conservation of mass (Equation 1), and since the taller loops expand more quickly, this effect is more pronounced than it is in shorter loops.

Finally, we briefly examine the evolution of the irradiance of the spectral lines at various temperatures. Figure 11 shows this comparison for the five loops. As before, we have normalized the total volume of each loop to be equal. In general, the tallest loop has the largest peak intensity because it has the largest coronal volume. In the cooler lines, this peak occurs when the loop cools through the line's formation temperature. However, before then, the short, wide loops have the highest densities (compare the apex densities in Figure 10), so they are brightest in transition region lines like O VI 1032 Å and Fe IX 171 Å. In flaring lines like Fe XXIII 133 Å, however, short, wide loops are the brightest in peak intensity, since the intensity decreases with time as the loop cools.

6. Conclusions

In this work, we have briefly examined two geometrical assumptions that are commonly used in hydrodynamic modeling of coronal loops. It is often assumed in field-aligned simulations that coronal loops are semi-circular with constant cross-sectional area. Observations of loop widths suggest that coronal loops only show minimal expansion, but the decrease of the magnetic field with height in the corona implies that there ought to be an expansion. It is not clear how to resolve this discrepancy, but the comparison of simulations and observations may offer insight to better understand this problem. On the other hand, many loops are very clearly not semi-circular, and are often very eccentric, but the impact of this on loop dynamics has been not been critically examined.

We first examined the assumption of a non-uniform cross-sectional area in Section 3. This has been touched upon by a few authors (Emslie et al. 1992; Mikić et al. 2013; Froment et al. 2018; Winebarger et al. 2018; Reep et al. 2020; Cargill et al. 2021) and found to be important for numerous reasons, such as impacting observed Doppler shifts or modifying the thermal conduction profiles. However, this has not been universally adopted in loop simulations; uniform cross-sectional areas are commonly assumed. The primary reason for this is that it

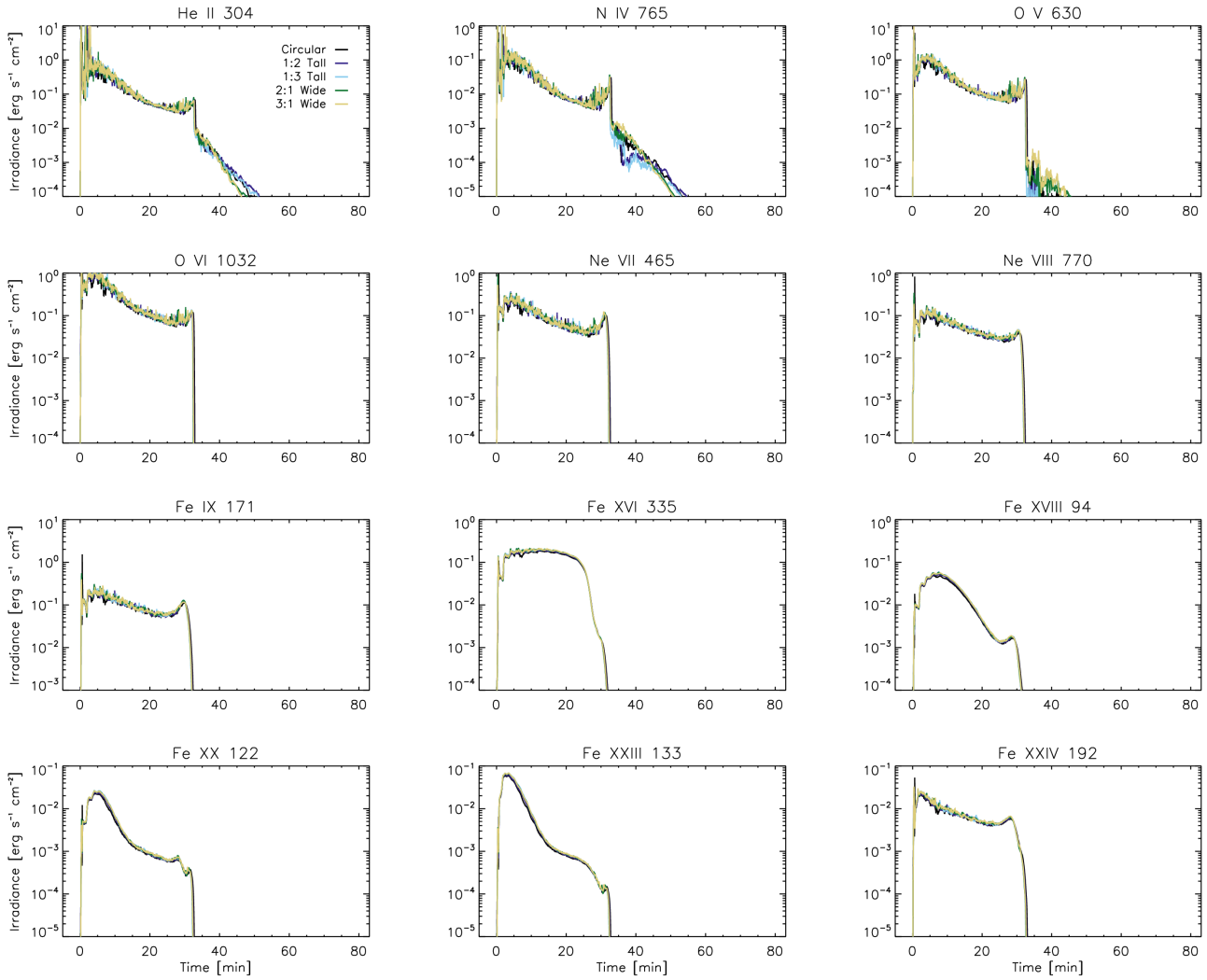

Figure 8. The synthetic irradiance for 12 lines as might be seen by SDO/EVE. The loops were assumed elliptical, as annotated, with a uniform cross-sectional area. The ellipticity of the loops has a negligible effect on the line intensities.

is not at all apparent how the expansion profile varies with height, what its magnitude is, or what the rate of expansion with height is. We have not attempted to reproduce any observations in this paper, but instead focus on simply understanding how an expansion would impact dynamics. We find that an area expansion significantly increases the time for a loop to cool and drain, increases upflow durations and localizes upflows near the footpoints, and suppresses sound waves. Despite the changes in the hydrodynamics, we still did not find any coronal condensation events in any of the simulations (see also Reep et al. 2020). Synthetic line intensities are impacted both directly from the change in volume with height and indirectly through the effects on the density and ionization profiles. Additionally, the location and rate of the expansion is important. When the expansion is localized near the transition region, the cooling time and draining time are both reduced compared to a more gradual expansion of similar magnitude. It is fundamentally important therefore to use a cross-sectional area expansion in loop simulations, both for understanding the hydrodynamics and the radiative output. Many previous results ought to be critically reexamined in the context of expanding cross-sections.

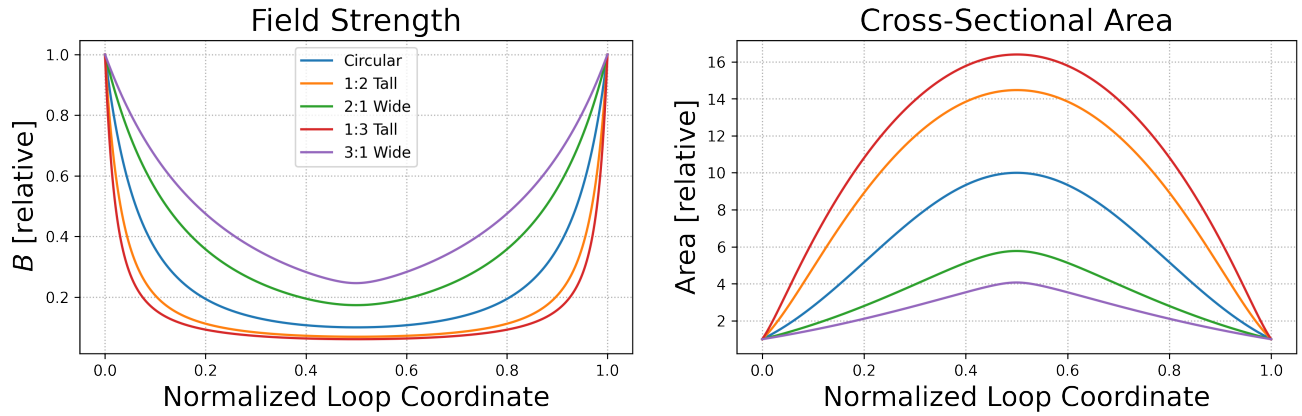

Figure 9. The magnetic field variation, $B \propto \frac{1}{r^2}$, (left) and corresponding cross-sectional area (right) in the five loops examined in this section. The circular case (blue) has an expansion of precisely 10 from footpoint to apex, while the taller loops (orange and red) have a larger expansion and wider loops (green and purple) a smaller expansion.

Additionally, observations are required to further constrain the magnitude and rate of expansion.

The assumption of semi-circular loops, that is, an eccentricity of 0, is almost universally used in the literature. We have examined this assumption in Section 4 by varying the gravitational acceleration parallel to the loop in accordance with both tall loops (vertical semi-major axis) and wide loops (horizontal semi-major axis). We have found that the draining time of the loops is reduced in tall loops compared to the semi-circular case since gravity is weakened with height, whereas the draining time is increased in wide loops for the opposite reason. The cooling times, peak temperatures, and peak densities are mostly unaffected. As a result, the spectral line intensities are mostly unaffected. In other words, this assumption is relatively unimportant in impulsively heated loop simulations.

Finally, in Section 5, we have combined the two geometrical assumptions, and examined elliptical loops with an area expansion that scales with height above the solar surface, such that the magnetic field $B \propto \frac{1}{r^2}$, or $A \propto r^2$. In this case, we do find that the dynamics are somewhat affected. A circular loop has the longest cooling time, which, when compared with the results of Section 3, indicates that the rate of expansion $\frac{dA}{ds}$ is also an important factor.

We emphasize that a non-uniform cross-sectional area strongly impacts all of the hydrodynamic quantities, and therefore the radiation as well. We note that in none of the simulations here do we find coronal condensation events characteristic of coronal rain, reiterating the result of Reep et al. (2020). While the geometry does impact the basic quantities, it still appears that there needs to be some secondary heating term to produce rain. In general, simulations of coronal loops must include area expansion to accurately simulate the dynamics, particularly the cooling of loops. Observations, additionally, are required to constrain the magnitude, rate, and location of the expansion to better inform the simulations.

The authors were supported by a NASA Heliophysics Supporting Research Grant, number NNH19ZDA001N, and by the Office of Naval Research 6.1 Support Program. This research benefited from discussions held at a meeting at the International Space Science Institute, in

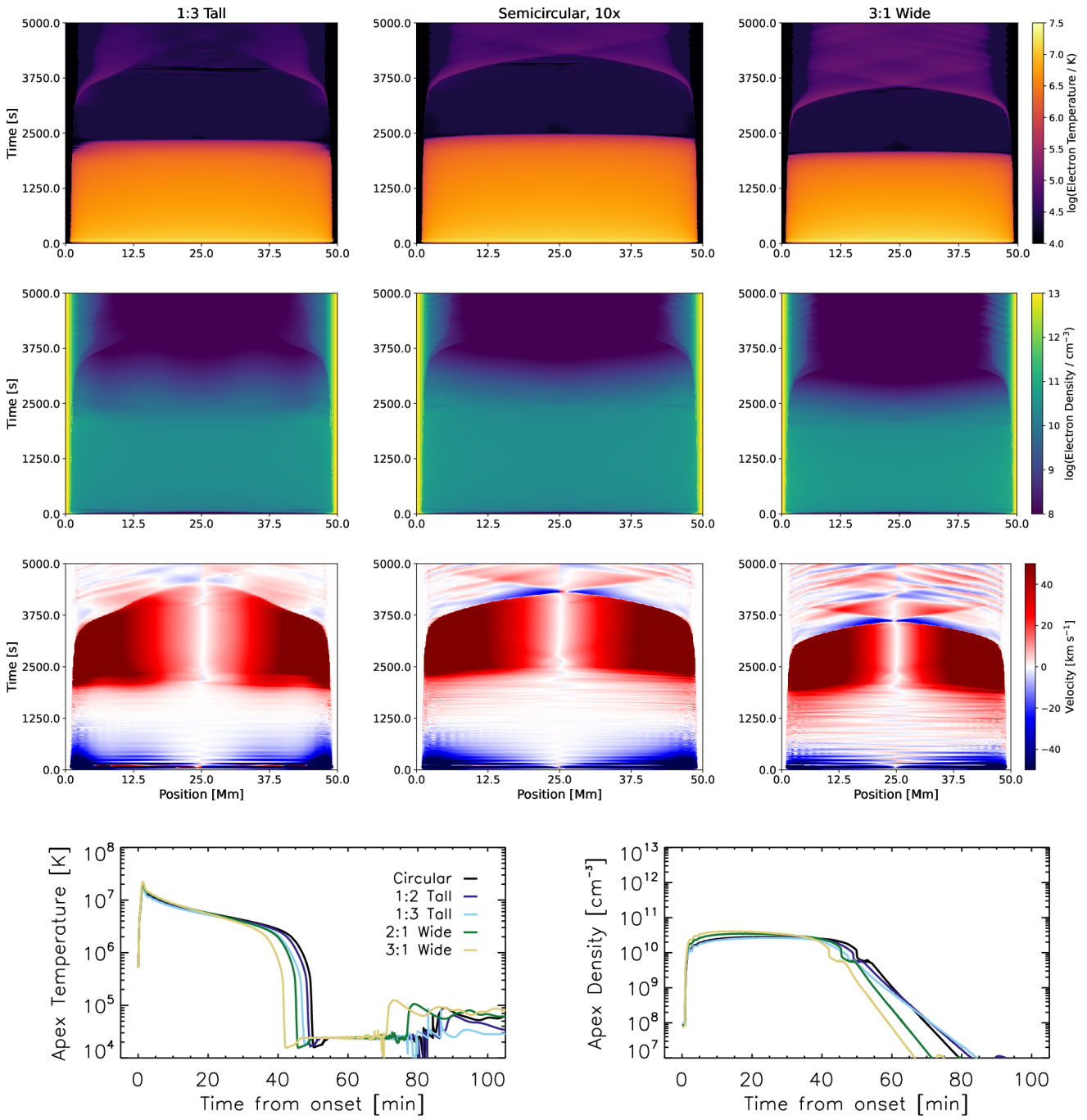

Figure 10. The overall hydrodynamic evolution in a set of elliptical flaring loops with expanding area, corresponding to the gravity and area profiles in Figures 14 and 9. The left column shows a tall loop (1:3), the center a circular loop (1:1), and the right a wide loop (3:1). The wide loop drains and cools the fastest, while the circular loop cools the slowest and the tall loop drains the slowest. The evaporative up-flows last longer in the tall case, and are also more confined near the footpoints, consistent with it having a somewhat larger area expansion.

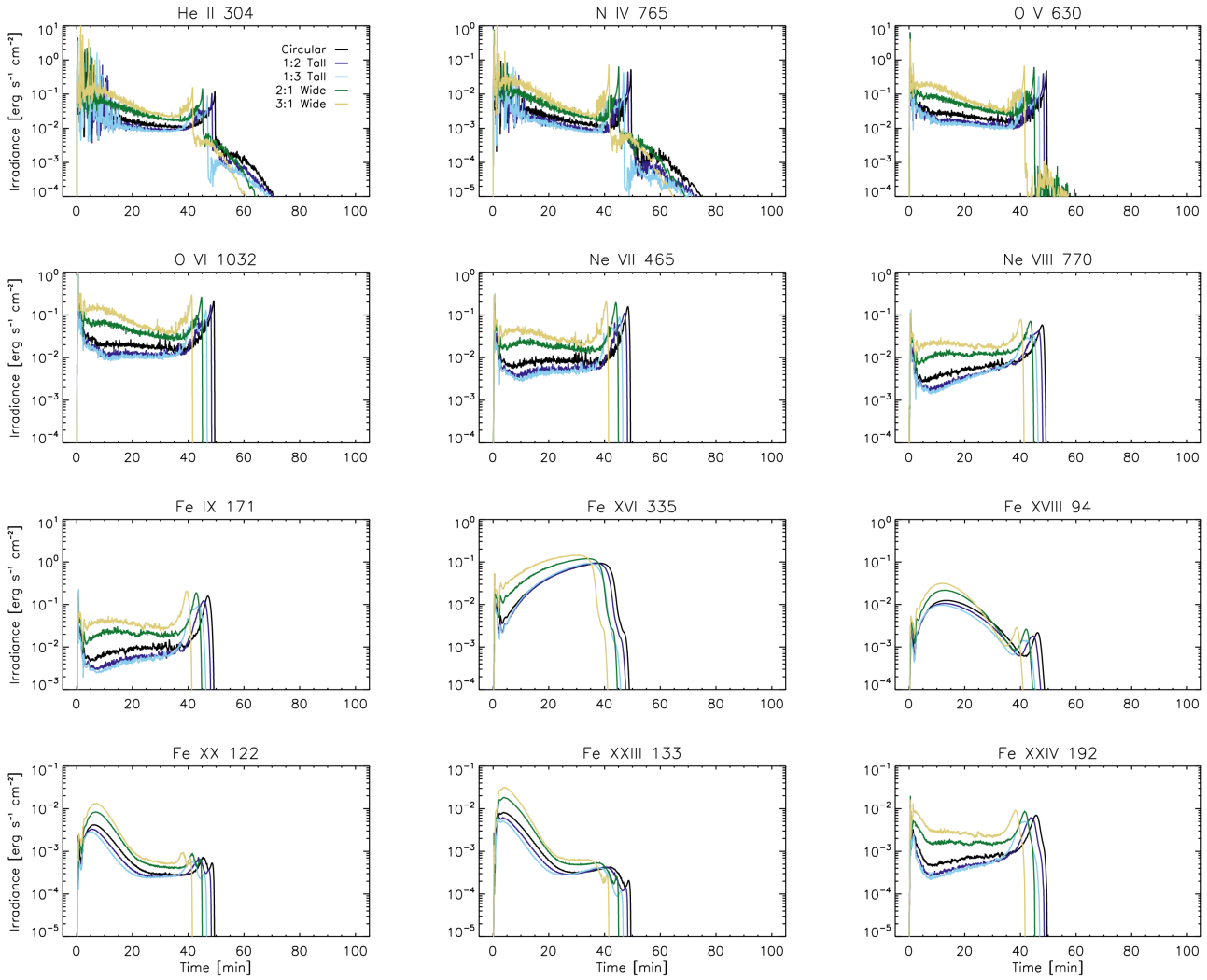

Figure 11. The synthetic irradiance for 12 spectral lines as might be seen by SDO/EVE, corresponding to the loops in Figure 10. The cooling times are affected by the ellipticity here, and the tall loops, which have the largest volume, are typically the brightest. The effect is relatively muted, though.

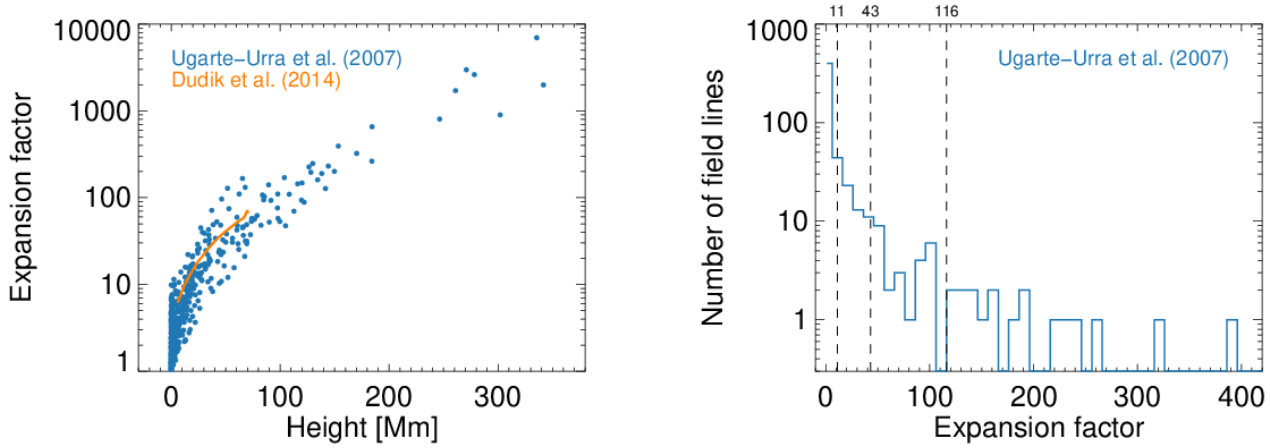

Figure 12. Expansion factors of closed magnetic field lines in two potential field extrapolations of a flare-active and a quiescent active region from Ugarte-Urra et al. (2007) and Dudík et al. (2014). The dashed lines show a reference to expansion factors used in Section 3.1.

Bern, Switzerland, led by Drs. Vanessa Polito and Graham Kerr.

Appendix

A. Observationally-Inferred Area Expansion Factors

One consequence of the conservation of magnetic flux is that the cross-sectional area of loops in the corona must expand as the magnetic field decreases in the solar atmosphere. Figure 12 shows the range of expansion factors derived from magnetic field extrapolations of two active regions.

Blue circles correspond to a current-free (potential) extrapolation of a MDI (Scherrer et al. 1995) photospheric magnetogram of the flare-active active region NOAA 9077 (2000 July 14, 09:36 UT). This extrapolation was part of a study of the magnetic topology of 26 CME events (Ugarte-Urra et al. 2007). The expansion factor was calculated from the ratio between the maximum and minimum magnetic field strength for 541 closed field lines within the Cartesian domain.

The orange curve corresponds to the potential magnetic field extrapolation of a high-resolution *Hinode*/SOT magnetogram (Tsuneta et al. 2008) of the quiescent active region NOAA 11482 (2012 May 18, 21:30 UT) presented in the investigation of area expansion factors by Dudík et al. (2014). The expansion factor values are those described as "height-averaged values of $\Gamma(Z)_{X,Y}$ Green's function extrapolation" for closed coronal loops, in Figure 3 of that paper.

The right panel of Figure 12 shows a histogram of the expansion factors in the NOAA 9077 dataset with a reference to the expansion factor values used in Section 3.1 of the present paper: 1, 11, 43, 116. These numbers cover 96% of the loops in this extrapolation.

B. Gravitational Acceleration in Elliptical Loops

In order to examine how ellipticity affects loop hydrodynamics, we must modify the gravitational acceleration $g_{\parallel}(s)$ parallel to the loop coordinate s. We consider five cases, shown in the cartoon in

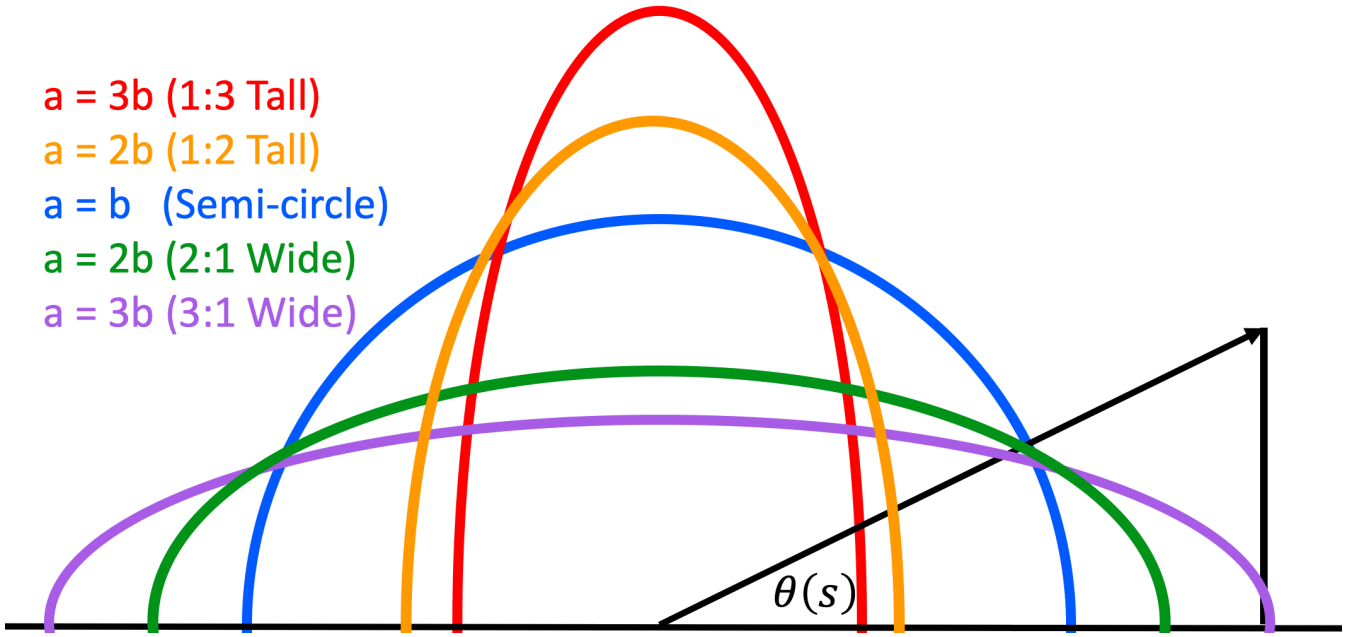

Figure 13. A cartoon of the ellipse geometries assumed in this work. We use two tall loops, with semi-major axis a is oriented radially outwards from the solar surface (red and orange), a semi-circular loop (blue), and two wide loops, with semi-major axis oriented parallel to the solar surface (green and purple). (Not perfectly to scale.)

Figure 13. In addition to the standard semi-circular case (blue), we use cases with semi-major axis a oriented either radially outwards from the solar surface ("tall loops") or parallel to it ("wide loops").

As a function of the angle θ relative to the ellipse center, the acceleration parallel to s at a given height along a loop is

$$g_{\parallel} = g_{\odot}\left(\frac{R_{\odot}}{R_{\odot} + h\sin\theta}\right)^2 \cos\theta \tag{B1}$$

where $g_{\odot}$ is the solar surface gravity, $R_{\odot}$ the solar radius, and h the maximum height above the solar surface. To determine the maximum height h for a given loop length, we use the approximation for an ellipse's circumference given by Ramanujan (1914):

$$C = \pi\left((a+b) + \frac{(a-b)^2}{10(a+b) + \sqrt{a^2 + 14ab + b^2}} + \epsilon\right) \tag{B2}$$

where a and b are the semi-major and semi-minor axes, and ϵ is an error term of order ak^{20} for k the eccentricity. If the semi-major axis a is oriented vertically, then we can write the height $y = a\sin\theta$ and $x = b\cos\theta$ (if oriented horizontally, we would swap a and b). In order to then calculate the field-aligned gravitational acceleration, we must convert between θ and the loop coordinate s used

by HYDRAD. From the Pythagorean theorem, we have

$$\begin{aligned} ds &= \left[\left(\frac{dx}{d\theta}\right)^2 + \left(\frac{dy}{d\theta}\right)^2\right]^{\frac{1}{2}} d\theta \\ &= \left[b^2 \sin^2\theta + a^2 \cos^2\theta\right]^{\frac{1}{2}} d\theta \\ &= a\Big((1-k^2)\sin^2\theta + \cos^2\theta\Big)^{\frac{1}{2}} d\theta \end{aligned} \tag{B3}$$

So we can integrate numerically

$$s(\theta) = a\int_{\theta_0}^{\theta_1} \Big((1-k^2)\sin^2\theta + \cos^2\theta\Big)^{\frac{1}{2}} d\theta \tag{B4}$$

We can then use this to convert between s and θ, and since we know $g_\parallel(\theta)$, we have the gravitational acceleration as a function of loop coordinate s for any specified eccentricity and loop length.

Figure 14 shows an example calculation for 50 Mm semi-elliptical loops. At top left, we show the acceleration along the loop coordinate $s(\theta)$, while the top right plot shows the acceleration as a function of θ, and the bottom plot shows the conversion between s and θ for clarity. The blue line shows the acceleration for the semi-circular case, the most common assumption in loop models, which is a perfect sine wave. The orange and red cases show tall loops, where the semi-major axis is oriented vertically, with $a = 2b$ and $a = 3b$ respectively. The green and purple cases likewise show wide loops, semi-major axis oriented horizontally, $a = 2b$ and $a = 3b$ respectively. It is clear that in tall (wide) loops the gravitational acceleration parallel to the field is reduced (increased) relative to the semi-circular case.

References

Allred, J. C., Alaoui, M., Kowalski, A. F., & Kerr, G. S. 2020, ApJ, 902, 16

Aschwanden, M. J. 2009, SSRv, 149, 31

Asplund, M., Grevesse, N., Sauval, A. J., & Scott, P. 2009, ARA&A, 47, 481

Auchère, F., Froment, C., Soubrié, E., et al. 2018, ApJ, 853, 176

Bian, N. H., Watters, J. M., Kontar, E. P., & Emslie, A. G. 2016, ApJ, 833, 76

Bradshaw, S. J., & Cargill, P. J. 2013, ApJ, 770, 12

Bradshaw, S. J., & Mason, H. E. 2003, A&A, 401, 699

Cargill, P. J., Bradshaw, S. J., Klimchuk, J. A., & Barnes, W. T. 2021, MNRAS, doi:10.1093/mnras/stab3163

Carlsson, M., & Leenaarts, J. 2012, A&A, 539, A39

Del Zanna, G., Dere, K. P., Young, P. R., & Landi, E. 2021, ApJ, 909, 38

Dere, K. P., Landi, E., Mason, H. E., Monsignori Fossi, B. C., & Young, P. R. 1997, A&AS, 125, 149

Dudík, J., Dzifčáková, E., & Cirtain, J. W. 2014, ApJ, 796, 20

Emslie, A. G. 1978, ApJ, 224, 241

Emslie, A. G., Li, P., & Mariska, J. T. 1992, ApJ, 399, 714

Froment, C., Auchère, F., Mikić, Z., et al. 2018, ApJ, 855, 52

Gary, G. A. 2001, SoPh, 203, 71

Golub, L., Deluca, E., Austin, G., et al. 2007, SoPh, 243, 63

Handy, B. N., Acton, L. W., Kankelborg, C. C., et al. 1999, SoPh, 187, 229

Hawley, S. L., & Fisher, G. H. 1994, ApJ, 426, 387

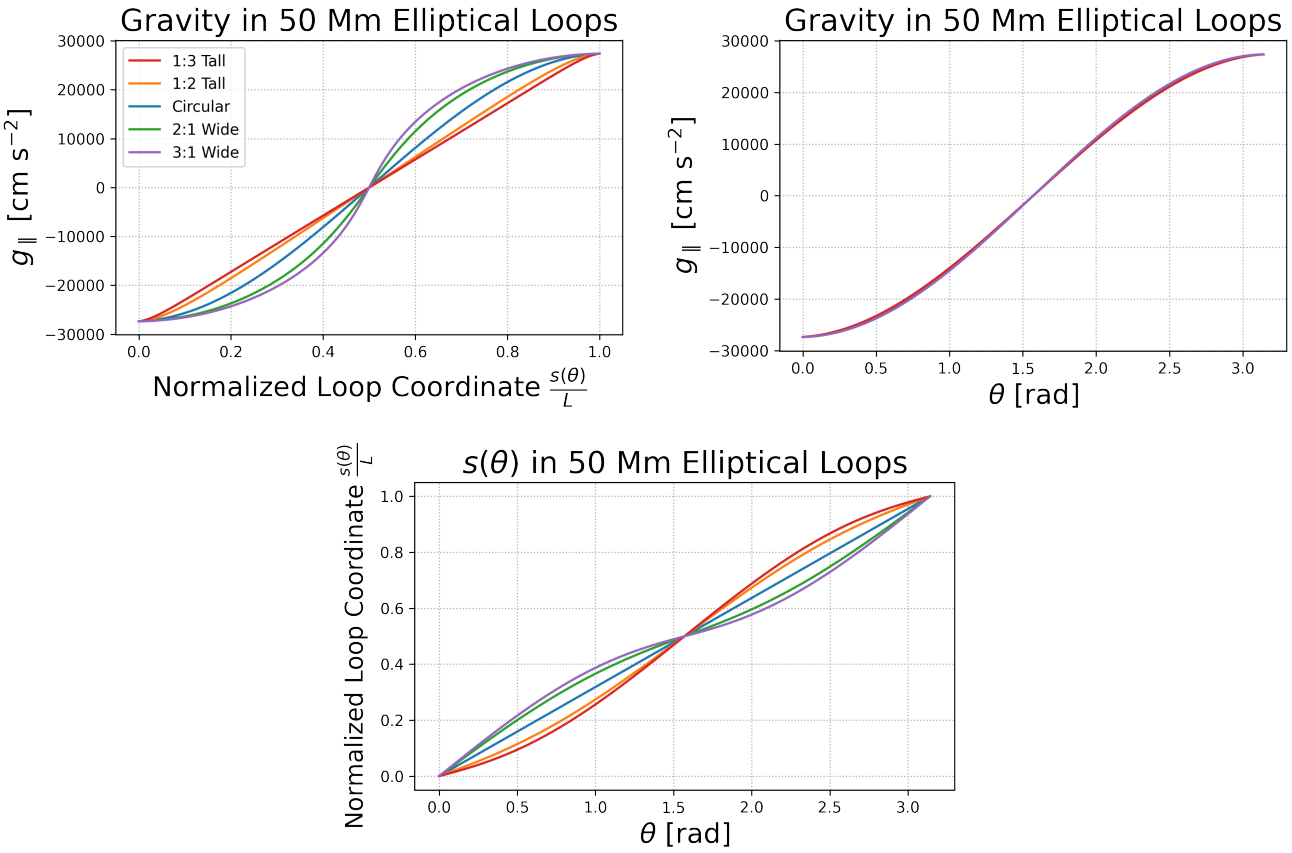

Figure 14. The parallel gravitational acceleration in 50 Mm semi-elliptical loops, as a function of position along the loop $s(\theta)$ (top left) and a function of θ (top right). At bottom, the relation between s and θ is shown explicitly for reference. The blue line shows the semi-circular case. The orange and red cases show tall loops, semi-major axis oriented radially outwards from the solar surface, $a = 2b$ and $a = 3b$ respectively. The green and purple cases similarly show wide loops, semi-major axis oriented parallel to the solar surface, $a = 2b$ and $a = 3b$.

Jing, J., Xu, Y., Cao, W., et al. 2016, Scientific Reports, 6, 24319

Klimchuk, J. A. 2000, SoPh, 193, 53

Klimchuk, J. A., & DeForest, C. E. 2020, ApJ, 900, 167

Lee, K.-S., Hara, H., Watanabe, K., et al. 2020, ApJ, 895, 42

Lemen, J. R., Title, A. M., Akin, D. J., et al. 2012, SoPh, 275, 17

Mikić, Z., Lionello, R., Mok, Y., Linker, J. A., & Winebarger, A. R. 2013, ApJ, 773, 94

Pelouze, G., Auchère, F., Bocchialini, K., et al. 2020, A&A, 634, A54

Pesnell, W. D., Thompson, B. J., & Chamberlin, P. C. 2012, SoPh, 275, 3

Qiu, J., & Longcope, D. W. 2016, ApJ, 820, 14

Ramanujan, S. 1914, Quarterly Journal of Mathematics, 45, 350

Reep, J. W., Antolin, P., & Bradshaw, S. J. 2020, ApJ, 890, 100

Reep, J. W., Polito, V., Warren, H. P., & Crump, N. A. 2018, ApJ, 856, 149

Reep, J. W., Siskind, D. E., & Warren, H. P. 2021, arXiv e-prints, arXiv:2110.06310

Scherrer, P. H., Bogart, R. S., Bush, R. I., et al. 1995, SoPh, 162, 129

Scullion, E., Rouppe van der Voort, L., Antolin, P., et al. 2016, ApJ, 833, 184

Tsuneta, S., Acton, L., Bruner, M., et al. 1991, SoPh, 136, 37

Tsuneta, S., Ichimoto, K., Katsukawa, Y., et al. 2008, SoPh, 249, 167

Ugarte-Urra, I., Warren, H. P., & Winebarger, A. R. 2007, ApJ, 662, 1293

Ugarte-Urra, I., Winebarger, A. R., & Warren, H. P. 2006, ApJ, 643, 1245

Vernazza, J. E., Avrett, E. H., & Loeser, R. 1981, ApJS, 45, 635

Warren, H. P., Kim, D. M., DeGiorgi, A. M., & Ugarte-Urra, I. 2010a, ApJ, 713, 1095

Warren, H. P., Winebarger, A. R., & Brooks, D. H. 2010b, ApJ, 711, 228

Watko, J. A., & Klimchuk, J. A. 2000, SoPh, 193, 77

Winebarger, A. R., Lionello, R., Downs, C., Mikić, Z., & Linker, J. 2018, ApJ, 865, 111

Winebarger, A. R., & Warren, H. P. 2004, ApJL, 610, L129

Woods, T. N., Eparvier, F. G., Hock, R., et al. 2012, SoPh, 275, 115

Wuelser, J.-P., Lemen, J. R., Tarbell, T. D., et al. 2004, in Society of Photo-Optical Instrumentation Engineers (SPIE) Conference Series, Vol. 5171, Telescopes and Instrumentation for Solar Astrophysics, ed. S. Fineschi & M. A. Gummin, 111–122

Zhu, C., Qiu, J., & Longcope, D. W. 2018, ApJ, 856, 27